Journal Title
XX(X):1–13

DOI: 10.1177/ToBeAssigned
www.sagepub.com/
SAGE

Modelling of Fire-Suppressant Injection into Engine Nacelle for Various Flight Regimes

Mohamed Arif MOHAMED, Tze How NEW and Bing Feng NG

Abstract

In this study, the injection of Halon 1301, an effective fire-suppressing agent, into a helicopter engine nacelle is modelled to provide insights into dispersion behaviour alongside complex flow physics. The injection velocity as well as the mass flow rate were retrieved via a 1-D pipe model to simulate nitrogen-pressurized flow of Halon 1301 in a four-branch pipe system. The Discrete Phase Model (DPM) in ANSYS Fluent was then used to model the injection of Halon 1301 into an engine nacelle. To simulate engine operation conditions in forward flight and hover regime, external boundary conditions were prescribed to the pressure inlets in the nacelle. When Halon 1301 is injected into the engine bay via the first pair of injection points, the droplets immediately reach their boiling point of 215 K. This resulted in an explosive-dispersion behaviour with a cone angle in the range of 80° to 90°. As the agent evaporates, the engine cools and another pair of injection points located at the rear of the engine is subsequently activated, helping to cool the engine further. The two flight regimes considered namely, hover and forward flight, showed contrast in flow dynamics which affected the cooling of the engine as well as the spray dynamics. In particular, the forward flight case showed more recirculation zones compared to the hover case. The volume concentrations of Halon 1301 were plotted for eleven probe points within the nacelle, and it was observed that two locations showed traces of low concentration levels.

Keywords
Helicopter fire safety, Halon 1301, computational fluid dynamics, engine nacelle

I: Introduction

The breakout of a fire on an aircraft can be catastrophic especially if it occurs in the engine nacelle. This could potentially lead to the aircraft losing thrust. In the engine bay itself, a fire (more typically, a spray fire) can occur when flammable fluids emanating from a leakage comes into contact with hot machinery components. When the flaming fluid seeps into the lower cavities of the nacelle and starts a pool fire, it can be very hard to extinguish[1]. One of the ways to put out a fire in the nacelle is to cause a flooding of a fire suppressing agent within the affected areas[2]. The process of extinguishing a fire in an engine nacelle starts with the activation of the release valve in a fire-extinguishing system connecting the storage bottle to the pipelines.

Bromotrifluoromethane, commonly known as Halon 1301, is an effective agent to put out fires. A concentration of 6% by volume for a duration of 0.5 s is sufficient to extinguish a fire[3]. Unfortunately, Halon 1301 is known to be destructive to the stratospheric ozone and the 2010 Montreal Protocol[4] mandates the cessation of Halon 1301 production. As a consequence, limited studies and experiments on the effectiveness of Halon 1301 were conducted despite their continued usage. This however does not lower the importance of the agent as many aircraft are still using them today. Alternatives to Halon 1301 like Novec1230 has been approved by the Federal Aviation Administration but requires careful design of the nozzles for an efficient distribution (in an airplane cargo cabin).[5] Although it is possible to use Computational Fluid Dynamics (CFD) to solve for the agent flow through the pipe networks, the computational overheads incurred would be high. The recourse would be to develop a one-dimensional (1D) pipe flow model where the outputs would be used to supply the conditions needed for the nozzles for the spray simulations in the engine bay.

The existing pipe-line modelling methods for Halon 1301 are generally proprietary and primarily empirically based. Only a handful of 1D modelling codes have been developed and are available in the open literature to predict the flow of nitrogen-pressurized Halon 1301 in fire extinguishing systems[6–8]. Snegirev et al.[9] for example developed a discharge model for a pipe flow system containing halon and nitrogen where steady ordinary differential equations (ODEs) are solved for the bottle and nozzle outlets while transient ODEs are solved for the bottle equations. The mass flow rate is computed from solving an eigenvalue problem. Snegirev et al. then used the results from the discharge model as boundary conditions for their CFD study and compared halon spray trajectory from a nozzle into a quiescent environment using different parameters. Kurokawa et al.[10] modelled Halon 1301 concentration inside an aircraft

School of of Mechanical and Aerospace Engineering, Nanyang Technological University Singapore
50 Nanyang Avenue, Singapore 639798

Corresponding author:
Bing Feng Ng, School of of Mechanical and Aerospace Engineering, Nanyang Technological University Singapore
50 Nanyang Avenue, Singapore 639798
Email: bingfeng@ntu.edu.sg

cargo using a lumped parameter approach. However, the methodology proposed failed to show spatial concentration non-uniformity.

CFD simulations have been performed using Halon 1301[9,11–13] but the application relating to an engine nacelle in realistic flight conditions are limited. As such, this paper presents a description of the modelling of Halon 1301 injection into an engine nacelle for a forward flight and a hover regime scenarios. Note that the current study focuses on the flow physics and concentration of Halon 1301. The modelling of fire using models like SMARTFIRE fire model [14] is not included in the investigations.

The intention of this paper is to provide a first approximation to the flow dispersion characteristics of Halon 1301 in an engine nacelle under different flight regimes for the purpose of fire-safety certification. The paper is spilt up into the following sections: Section II describes the 1-D pipe flow model that we developed, upon which results from the model are used as initial and boundary conditions for the follow-up CFD simulations. Section III discusses the CFD methodologies and boundary conditions prescribed for the spray simulations. The results are discussed in Section IV and we conclude the paper with the summary in Section V.

II: 1-D Pipe Model

An object-oriented programming approach in Python 3.7 was developed for the modelling of the 1-D pipe flow. This involved creating a thermophysical class (database) for Halon 1301 and Nitrogen, which are functions of temperature and pressure obtained from Elliott et al.[6], obtained via the Redlich-Kwong equation of state. The code was designed for the system shown in Figure 1. There were several assumptions used in developing the code that followed closely to Elliott et al.[6]. Firstly, the kinetic energy of the fluid leaving the bottle (where Halon 1301 is initially pressurized by nitrogen) was ignored, so that the energy balance on the bottle included only the enthalpies and internal energies of the fluids leaving the bottle. Next, the two-phase mixture of Halon 1301 (liquid and vapour), dissolved nitrogen and gaseous nitrogen that flowed out of the bottle was assumed to be a homogeneous mixture (a single-phase compressible fluid with a mixture density) and under the assumption of having uniform velocity. Lastly, the flow in the system was assumed adiabatic.

The calculations for the 1-D pipe model start from the bottle where Halon 1301 is pressurized with Nitrogen. The methodology involves a pressure-drop step where the mass of fluid that must be discharged in each step of pressure drop is calculated (refer to Figure 2). At each pressure step, the temperature of the fluid in the bottle is first guessed. Subsequently, both the pressure and the estimated temperature of the bottle are used to calculate the thermodynamic properties of the two-phase halon-nitrogen mixture, via the mixture properties. The estimated temperature is considered correct when the energy balance equation is satisfied. This is via an iterative process. The iterative process also involves the guessing of a mass flow rate leaving the bottle.

Once the correct flow rate is determined, the time required for the discharge of that flow rate can be computed (via the relationship of mass and flow rate). In addition, the mixture density is computed at each pressure step, allowing velocity to be calculated.

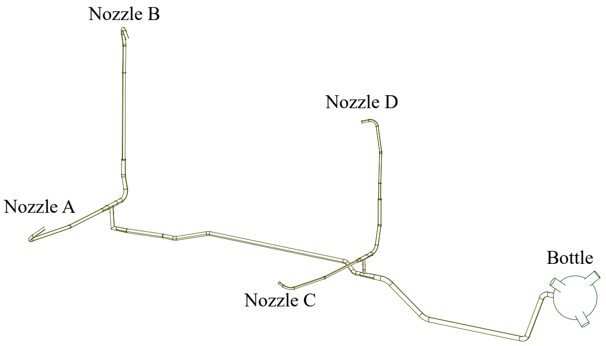

Figure 1. The geometry of the fire extinguishing system used for the current study.

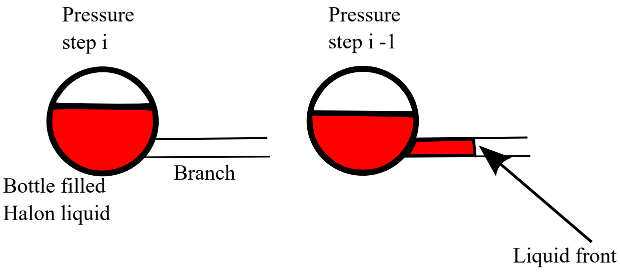

Figure 2. Pressure-drop step sequence of halon liquid discharged from bottle and into the connecting branch.

A. Multi-branch Pipe System

To accommodate for a multi-branch system, branch-area ratios at the junction are used. Consider the following three-branch system in Figure 3:

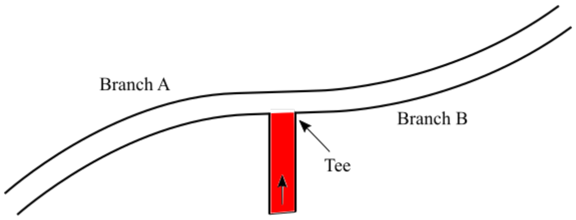

Figure 3. An example of a two branch system.

At the n^{th} pressure-drop step, where the liquid front is at the tee, it would have no preferred path if the cross sectional areas of Branch A and B are equal (note that branch areas for the current system are not always constant). Path preference would normally be a function of pressure via Bernoulli's equation but since both branches have almost atmospheric pressure at the pressure-drop step, this would not apply (note that pipe A and B are not filled, hence no pressurization). The distance traveled by the liquid front is computed via the following relations:

$$l_A = \frac{v_{\text{out}_n}}{A_{\text{Total}}} \frac{A_{\text{BranchA}}}{A_{\text{Total}}} \tag{1}$$

$$l_B = \frac{v_{\text{out}_n}}{A_{\text{Total}}} \frac{A_{\text{BranchB}}}{A_{\text{Total}}} \tag{2}$$

where v_{out_n} is the volume of fluid out of the bottle at the n^{th} pressure-drop step, A is the cross-sectional area of either Branch A or B as indicated in the subscript, and A_{Total} is the combined area of Branch A and B. l_A and l_B are the distance traveled by the liquid front in Branch A and B respectively.

B: Equivalent Pipe Length

The pressure losses in pipe flows can be computed *via* the Darcy-Weisbach formulation, which is a function the Darcy-Weisbach friction factor f related to Reynolds number for smooth pipes and pipe relative roughness [15]. For two-phase (gas-liquid) flows, f can be computed via correlations of single-phase flows[16], which is dependent on phase-related parameters such as vapour quality, mass flux, density, *etc.* for each phase[17–19]. One of the more direct approaches to estimating pressure loss *via* friction in pipe flows is through head loss Δh. The generalized form of Δh for straight pipes is

$$\Delta h = f_D \frac{L}{D} \frac{V_{\text{ave}}^2}{2g} \tag{3}$$

where f_D, L, D, V_{ave} and g are the friction factor, pipe length, diameter, average velocity and acceleration due to gravity, respectively. For a system with multiple pipe branches, additional losses come from pipe fittings, valves, elbows, etc. Δh would then be a function of the geometry of the fittings, Reynolds number and roughness. In a multi-branch system, L in Eq. (3) is replaced with an equivalent length. The equivalent lengths for pipes with bends, tees, valves, etc. can be obtained from standard lookup tables (see[20]). Prior to running the simulations for the system shown in Figure 1, the code was compared with simulations of Elliot et al[6] and showed that it was able to replicate the results reasonably well for a system without converging nozzles.

For the given system show in Figure 1, together with the initial bottle conditions displayed in Table 1, the mass flow rate at the four nozzles are computed and displayed in Figure 4. The sharp drops of mass flow rate at around 1.5 s for nozzles C and D and around 3.85 s for nozzles A and B are due to the fact that the liquid mixture of halon and nitrogen has been completely exhausted, and the system at those instances on wards worked with the gas phase of the mixture. This was also seen in the simulations of Yuan et al.[21] and Elliot et al[6].

Table 1. Initial bottle conditions.

Bottle Volume	983.224 cm^3
Bottle Pressure	2.482 MPa
Mass of Halon	0.857 kg
Bottle Temperature	293.15 K

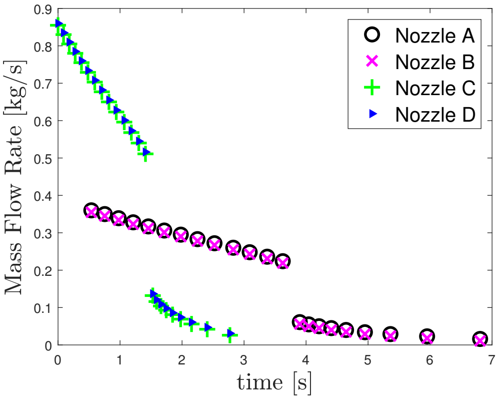

Figure 4. Transient mass flow rate at the four nozzles. The discontinuity indicates a change from liquid to vapour phase.

III: Computational Framework

A. Discrete Phase Model

In the current study, ANSYS Fluent was used to model the dispersion of Halon in the engine nacelle via the Discrete Phase Model (DPM), which allows for the modelling of the evaporation of a liquid. The discrete phase is solved through the Lagrangian method by tracking droplets/particles and allows the interchangeability of mass, momentum and energy between the dispersed and fluid phases. DPM requires certain size constraints in the cells adjacent to the injection points in a manner that allows for the particles to occupy at most 12% of the cell volume (discrete phase) with the rest of the cell being in the continuum phase [22].

The force balance on the particle is modelled as

$$m_p \frac{du_p}{dt} = m_p \frac{u - u_p}{\tau_r} + m_p \frac{g(\rho_p - \rho)}{\rho_p} + F \tag{4}$$

Here, the variables with subscript p represent the variables tied to the particle while m_p is particle mass, u is velocity, ρ is density, g is acceleration due to gravity and F is the external force . τ_r is a time scale defined as

$$\tau_r = \frac{\rho_p d_p^2}{18\mu} \frac{24}{C_d Re_d} \tag{5}$$

where d_p is particle diameter, μ is molecular viscosity C_d is drag and Re_d is particle Reynolds number. Lift forces can influence the trajectory of the particles in the presence of significant normal/cross-flow velocity gradients[23]. Due to the complex nature of the flow physics within the engine bay, this force has been included in the form of Saffman's Lift Force, expressed as

$$F_S = m_p \frac{2K\nu^{1/2}\rho d_{ij}}{\rho_p d_p (d_{lk} d_{kl})^{1/4}} (u - u_p) \tag{6}$$

where d_{ij} is the deformation tensor, ν is kinematic viscosity and K is a constant. The spray characteristics of fire extinguishing agents are normally induced by their thermodynamic parameters[24]. It is therefore necessary to include the energy equation for the modelling of Halon 1301 spray. The heat balance equation for the particle is given by

$$m_p c_p \frac{dT_p}{dt} = hA_P(T_\infty - T_p) + \frac{dm_p}{dt} h_{fg} + \epsilon_p A_p \sigma(\theta_R^4 - T_p^4) \tag{7}$$

where c_p, h, A_p and ϵ_p are particle specific heat, convective heat transfer coefficient, particle surface area and particle emissivity, respectively. σ is the Stefan-Boltzmann constant for radiation while T_∞ and θ_R are the local temperature in continuous phase and the radiation temperature, respectively. Latent heat is represented by h_{fg} and $\frac{dm_p}{dt}$ is the rate of evaporation. The convective heat transfer coefficient in Eq. (7) is computed through the following relationship[25]

$$\frac{hd_p}{k_\infty} = 2 + 0.6 Re_d^{1/2} Pr^{1/3} \tag{8}$$

where k_∞ is thermal conductivity of the continuous phase and Pr is the Prandtl number, given by $c_p\mu/k_\infty$. The term on the left hand side of Eq. (8) is the Nusselt number. The mass loss rate of the droplet is determined through its vapour diffusion rate away from the droplet surface. Note that this is for the range $T_{vap} \leq T_p < T_b$ where T_{vap} and T_b are droplet vaporization and boiling-point temperature, respectively. During vaporization, the mass loss rate is given by

$$m_p(t + \Delta t) = m_p(t) - \frac{k_c A_p M_{w,j}}{R}\left(\frac{p_{sat}(T_p)}{T_p} - X_j \frac{p}{T_\infty}\right)\Delta t \tag{9}$$

where $M_{w,j}$ is the molecular weight of species j, R is the universal gas constant, p_{sat} is saturation pressure and X_j is mole fraction of species j. k_c is the mass transfer coefficient and can be calculated from the Sherwood number Sh of the form

$$Sh = \frac{k_c d_p}{\mathscr{D}} = 2 + 0.6 Re_d^{1/2} Sc^{1/3} \tag{10}$$

where $\mathscr{D}$ is vapour diffusion coefficient and $Sc = \mu/\rho\mathscr{D}$ is the Schmidt number. Note that Eq. (9) is only applicable during vaporization. The mass of the droplet remains unchanged when $X_j > \frac{p_{sat}(T_p)}{T_p} / \frac{p_\infty}{T_\infty}$.

The boiling law applies when $T_p >= T_b$. When boiling point is reached, the particle size loss rate is given by

$$\frac{d(d_p)}{dt} = \frac{2k_\infty}{\rho_p c_p d_p}\left(2 + 0.6 Re_d^{1/2} Pr^{1/3}\right) \ln\left[1 + \frac{c_p(T_\infty - T_p)}{h}\right] \tag{11}$$

B: Injection Properties

Haenlein[26] defined four regimes of liquid disintegration, namely, Rayleigh-mechanism, first wind-induced, second wind-induced and atomization, which are developed based on the relationship between Reynolds number and the Ohnesorge number[27]. For the current study, the spray regime falls under atomization (based on computed Reynolds and Ohnesorge numbers), which is the immediate disintegration of the agent with no liquid core, primary or secondary breakups. Note that there are a few suggestions for the calculation of surface tension to compute the Ohnesorge number[6,28–30] and the method proposed by Lechner et al.[29] was used in this study.

The boiling point of Halon 1301 is 215.372 K. When released into the ambient air in this pressurized boiling state, the agent contains superheat[24] and is thermodynamically unstable, resulting in an explosive evaporation[9] (the reader is referred to Figure 1a in Snegirev et al.[9] to gain a perspective on the explosive nature of Halon 1301 when released into ambient air). The initial spray angle was estimated to be 90° and cylindrical in shape. In order to capture this phenomenon, the solid cone was used for the injection type with a spray angle of 70°. The drag law was set as non-spherical with a shape factor of 0.171. This was based on the acentric factor mentioned in[31]. The discrete random walk model was chosen for stochastic tracking.

The spread of particle size was modelled using The Rosin-Rammler distribution[32] (also classified as the Weibull distribution) and expressed as

$$1 - \mathscr{Y} = \exp\left(\frac{-x_0}{\mathscr{X}}\right)^q \tag{12}$$

where x_0 is droplet diameter and $\mathscr{Y}$ is the fraction of droplets with diameter less than x_0. $\mathscr{X}$ and q are constants. The exponent q is also known as the spread parameter that defines the uniformity of the spray[27]. A spread parameter of 1.8 was selected based on the recommendations of[9]. The minimum, maximum and mean droplet diameters were set to 10^{-6} m, 8×10^{-5} m and 5×10^{-5} m[9], respectively. The number of streams per injection was set to 300. The transient flow rate and velocity magnitude at the nozzles were obtained from the results of the 1D pipe flow model. The full description of the injection properties is described in Appendix A.

C: The Computational Model

Figure 5 shows the computational domain for the spray simulations. The four nozzles in Figure 5 are the locations where the injections of Halon 1301 liquid take place based on the time intervals computed by the 1D pipe flow model. The mesh was generated using a polyhedral meshing approach. Prior to the actual calculations, a grid convergence study was carried out. This was for three different meshes of sizes 3,914,422, 6,795,076 and 12,115,693 polyhedral cells. Four locations, labeled A1, A2, A3 and A4 in Figure 6 are used to compute the grid convergence index (GCI).

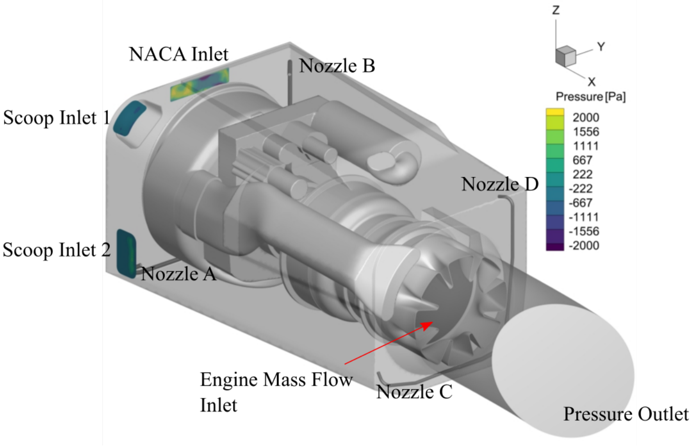

Figure 5. The engine bay with prescribed boundary conditions at Scoop inlets 1 and 2 as well as the NACA inlet.

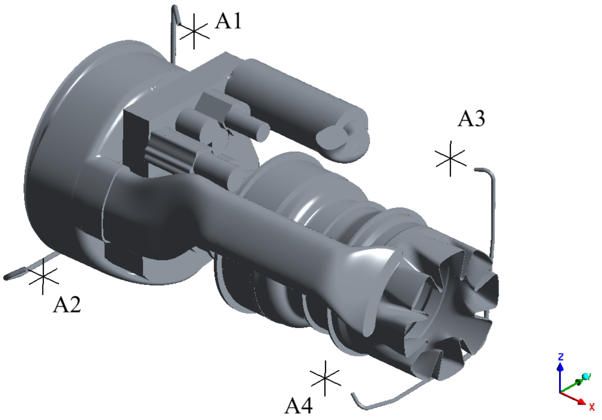

Figure 6. Points A1, A2, A3 and A4 at which GCI were computed.

GCI is a metric used for mesh independence tests (refer to[33] for a more detailed description). For this study, three meshes of different grid sizes were used to compute the GCI.

$$\mathrm{GCI} = F_s \frac{|\varepsilon_h|}{r^p - 1}, \quad \varepsilon_h = \frac{\phi_h - \phi_{rh}}{\phi_h} \tag{13}$$

where F_s=1.25 for a three-grid sequence of simulations, r is the grid refinement ratio and p is the order of the finite difference scheme. ϕ and ϕ_{rh} for this study represent the pressures at the designated points for mesh A and mesh B respectively (note that mesh B is the coarser grid). The results of the grid study at the four locations shown in Figure 6 are displayed in Table 2.

Table 2. Grid convergence study results at locations A1 - A4.

Number of polyhedral cells	GCI_{A1}	GCI_{A2}	GCI_{A3}	GCI_{A4}
3,914,422	-	-	-	-
6,795,076	1.131%	0.027%	0.088%	0.173%
12,115,693	0.385%	0.0001%	0.003%	0.0099%

Based on the results in Table 2, the mesh size of 6,795,076 cells was chosen for the actual simulations.

The realizable $k-\epsilon$ turbulence model with enhanced wall treatment and thermal-effects option was chosen for the simulations. The Semi-Implicit Method for Pressure Linked Equations (SIMPLE) method was employed for the updating of the pressure and the correction of the velocity fields per iteration. Spatial gradients were computed using the Least Squares Cell Based method. The second-order upwind scheme was selected for the transport equations and a second-order implicit scheme was used for the transient formulation.

D: Boundary Conditions

The no-slip boundary condition was selected for walls and the DPM boundary condition at the wall is set to trap. For a realistic simulation, a pressure field is prescribed at the two scoop inlets as well as the NACA inlet. The pressure fields were obtained from a previous external flow calculation. The virtual blade model (VBM) was used to compute the flow field of a helicopter in forward flight (refer to[34] for more details on the model). For this study, two flight regimes were considered namely, hover and forward flight. In order to show the how the two regimes affect the inlet boundary conditions, we have plotted the velocity distribution at the two scoop inlets and the NACA inlet for each case. This is shown in Figure 7. As shown, the two flight regimes not only show differences in velocity profiles but also displayed significant differences in magnitude. This is one of the reasons to have boundary conditions that relate to flight regimes, as opposed to uniform pressure or velocity at the inlets.

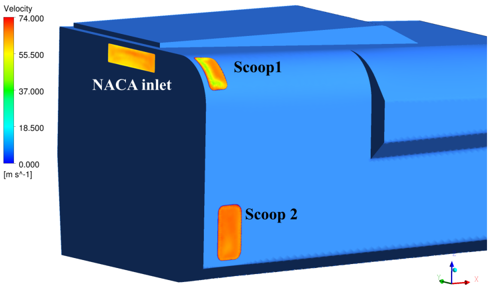

(a) Hover case

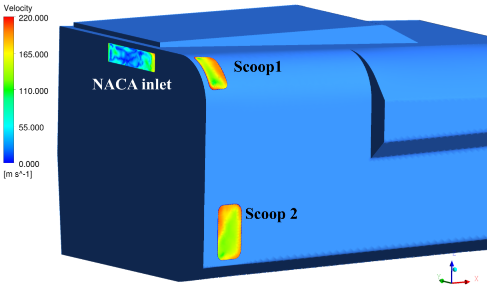

(b) Forward-flight case

Figure 7. Velocity distribution at the inlets for hover and forward-flight cases. Boundary conditions were retrieved from external flow simulations.

Figure 8 shows the velocity streamlines from the VBM simulations. The pressure and temperature fields from the results were then extracted and used as the boundary conditions for the spray simulations. The mass flow rate prescribed at the engine mass flow inlet was 6 kg/s with a temperature of 873.15 K. The ambient temperature set at the pressure outlet was 288.15 K. Prior to the actual unsteady spray simulations, a steady state solution was obtained with the aforementioned boundary conditions to generate an initial flowfield. The time-step used for the simulations is 0.005 s. The maximum y^+ was computed to be 16. It should be reminded that the enhanced wall function was used for the simulations and there is no necessity to reduce y^+ to 1.

IV: Results and Discussion

Figure 9 shows the first few bursts of the agent being injected into the engine nacelle for the hover and forward flight regime. The contours of temperature and particle diameter have been superimposed onto the engine and droplets, respectively to show the cooling effect of the sprays as well

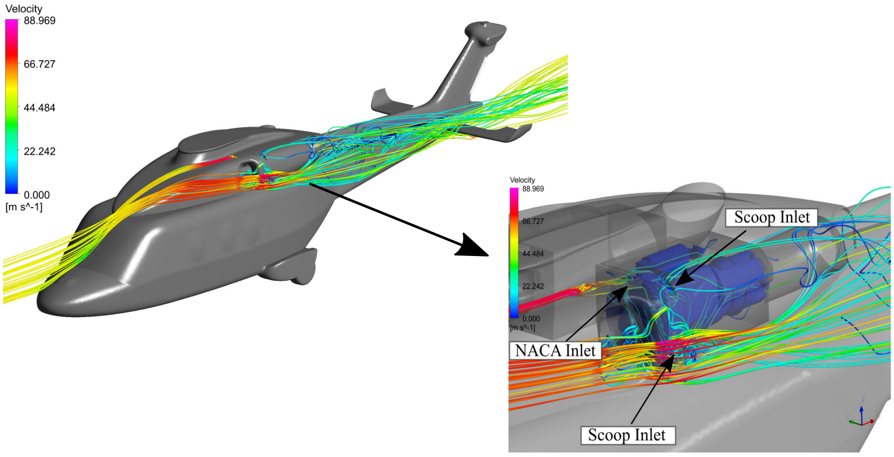

Figure 8. External flow simulations prior to the spray calculations. The simulations were performed to get the boundary conditions for the engine bay pressure inlets.

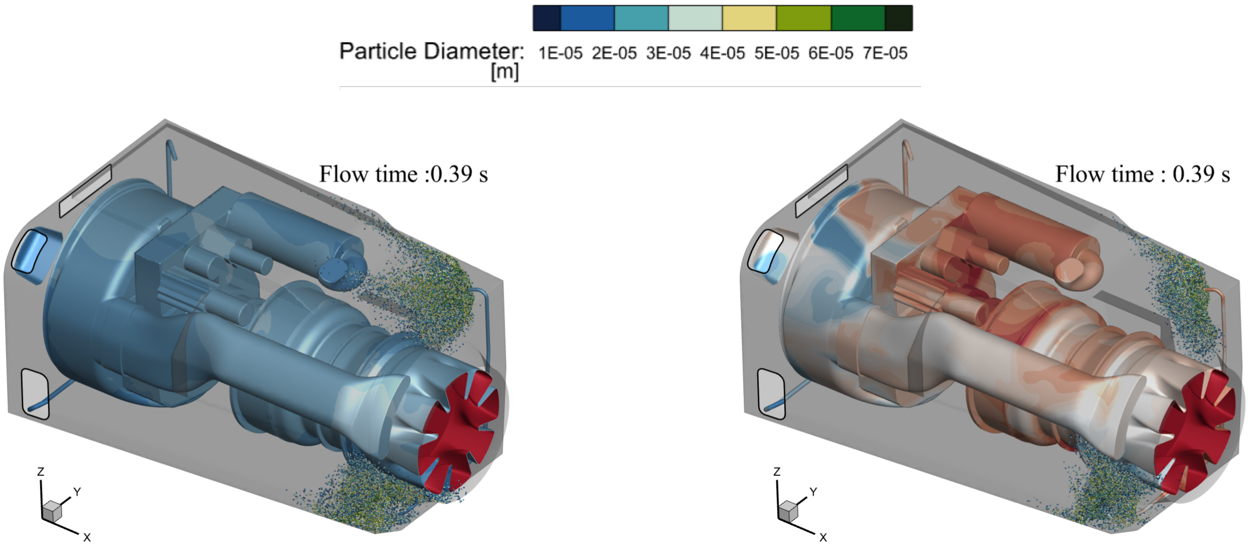

(a) Hover regime at 0.39s

(c) Forward flight regime at 0.39s

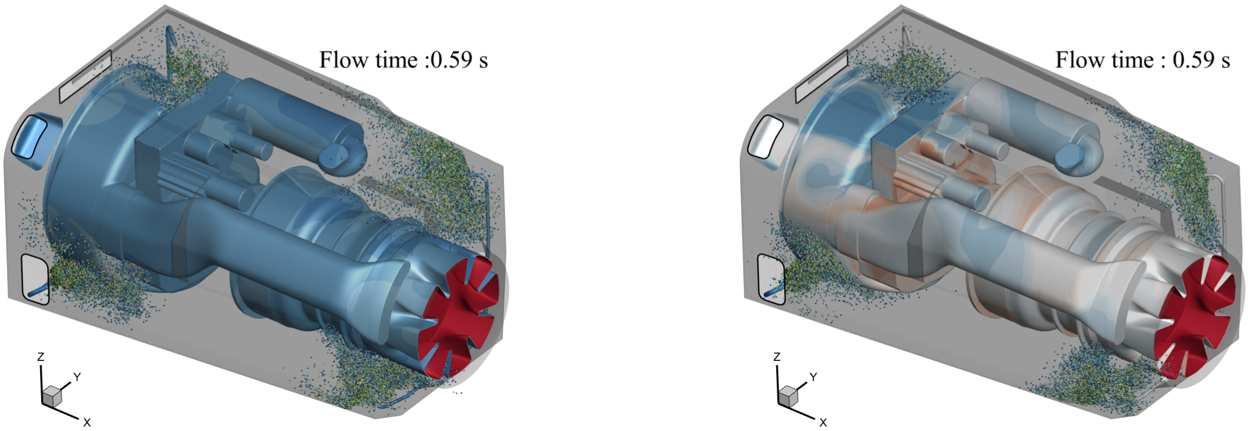

(b) Hover regime at 0.59s

(d) Forward flight regime at 0.59s

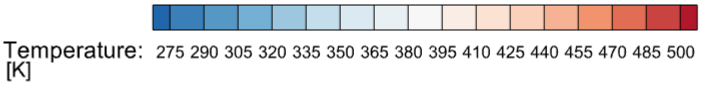

Figure 9. Trajectories of evaporating Halon 1301 for flow time 0.39 s and 0.59 s. The left column depicts cases where the boundary conditions are prescribed for a hover regime while the right column shows the conditions for a forward flight regime.

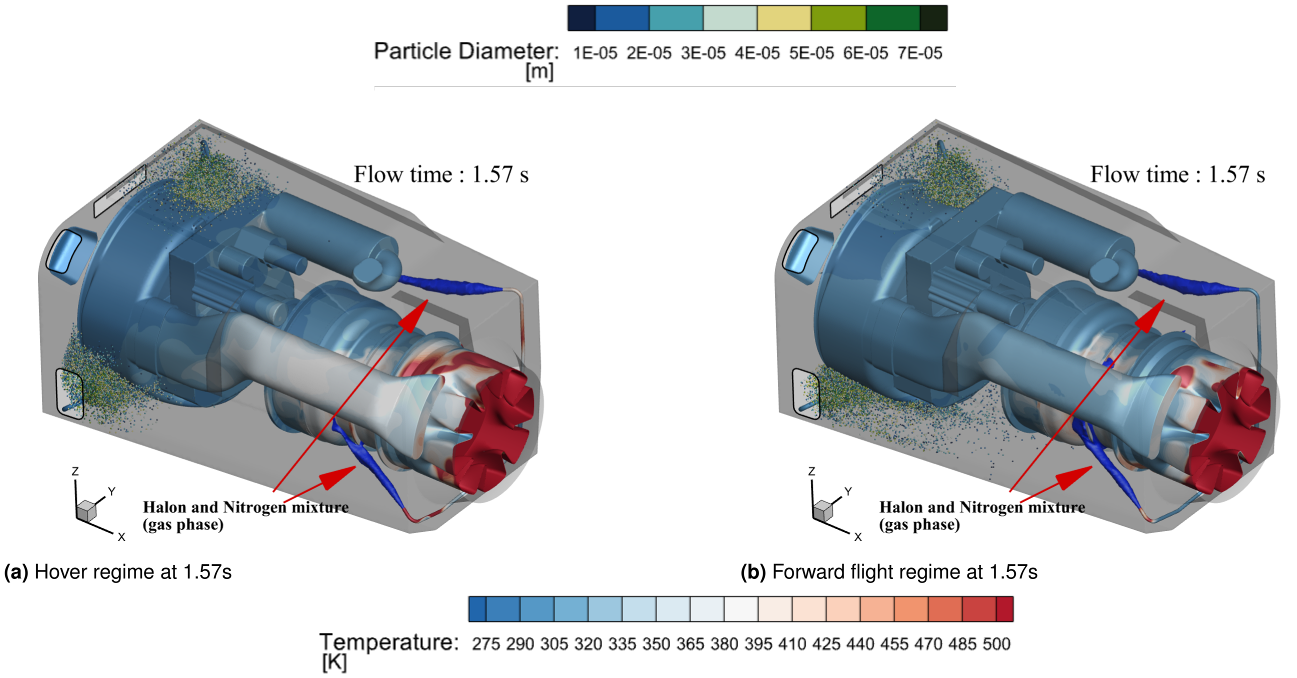

(a) Hover regime at 1.57s

(b) Forward flight regime at 1.57s

Figure 10. Trajectories of evaporating Halon 1301 for flow time 1.57 s. The gas phase mixture at flow time 1.57 s is shown emanating at Nozzles C and D (refer to Figure 5) . The left column depicts cases where the boundary conditions are prescribed for a hover regime while the right column shows the conditions for a forward flight regime.

as display the spectrum of particle size at different time intervals. At 0.39 s in Figure 9, only Nozzles C and D are active and it was observed that the scattering of the spray for the hover regime is more spread out in the negative X-direction in comparison to the forward flight regime. A jet expansion of the injected agent is expected due to the state of the liquid always being in superheat (boiling point of Halon 1301 is 215 K). At nozzle D for the forward flight case at 0.39 s, the spray trajectory of the droplets appears to be entrained towards the the eductor. This suction towards the positive X direction was not observed with the hover regime at the same time instance. This would suggest some form of a recirculation zone for the forward flight case in the vicinity of nozzle D. The evaporation of the droplets is dependent not only on temperature but the velocity/pressure field they are immersed in. In view of the fact that hot surfaces are a threat to fire safety when they are in contact with fuel vapour and air, wall temperatures within the nacelle must be given the same attention as the spray characteristics.

In the forward flight case at 0.39 s, higher temperature regions were observed on the engine surface compared to the hover regime. This is due to the boundary conditions set at the ventilation airflow through the engine bay. Note that the design of the NACA and scoop inlets is to provide cooling for the engine. The fire in an engine bay is usually of a turbulent diffusion flame stabilized behind an obstacle[35]. Ideally, airflow through the ventilation should be unidirectional to prevent flame propagation in the event of a fire outbreak. However, due to the design of the engine nacelle, turbulence is inevitable and its presence preclude homogeneity, which can lead to failure in the suppression of a fire. This justifies the inclusion of a realistic boundary condition at the inlets.

At 0.59 s, all four nozzles are active and there is an improvement in heat signature on the engine for the forward flight case from the previous instance at 0.39 s. The engine wall temperature distribution for the hover regime also shows a general cooling trend. With regards to spray trajectory, the evaporating droplets in the vicinity of nozzle D for the hover case continues to show a higher concentration compared to the forward flight regime. It should be made aware that the trap boundary condition was prescribed for the no-slip walls and that calculations for droplet trajectories are terminated when the droplets land on the surfaces. That is to say, the sparsity could be due to either the evaporation of the droplets or termination of them upon landing on walls. On close inspection in the vicinity of nozzle C, it appears that the halon spray is directed more towards the engine for the hover case compared to the forward flight case. It is also interesting to note that the region around nozzle B shows a higher concentration of droplets for the forward flight case.

When the flow time reaches 1.57 s (see Figure 10), nozzles C and D are no longer active, and are now emitting a mixture of halon and nitrogen in the gas phase (as computed by the 1D code). As highlighted in Figure 10 at 1.57 s, there is no jet expansion at nozzles C and D unlike the injection of halon liquid previously. The interesting observation here is the temperature distribution on the engine for both cases. The engine in the hovering case has a higher distribution of temperatures exceeding 380 K in comparison to the forward flight case. This distribution is not only within the vicinity of the mass flow inlet of temperature 873.15 K (refer to Figure 5 for location) but spreads more towards the negative X and Y direction. For the forward flight case, the engine has a more improved heat signature when compared to the flow time at 0.39 s.

The cooling streamtubes in Figures 11 and 12 are an indication of the transient nature within the engine nacelle. The contours of velocity magnitude are superimposed onto

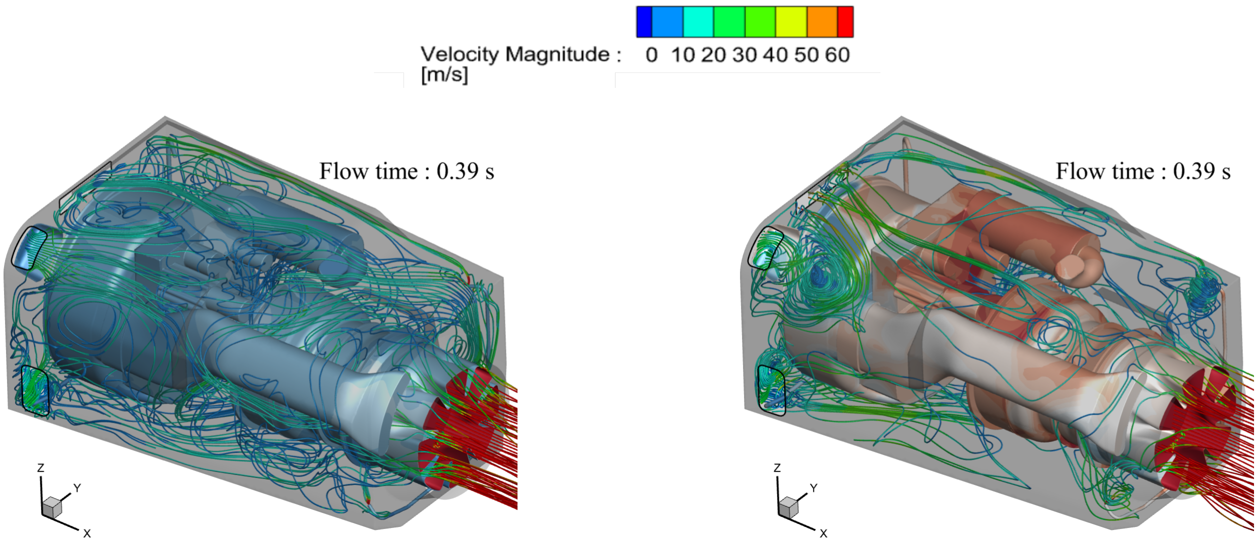

(a) Hover regime at 0.39s

(c) Forward flight regime at 0.39s

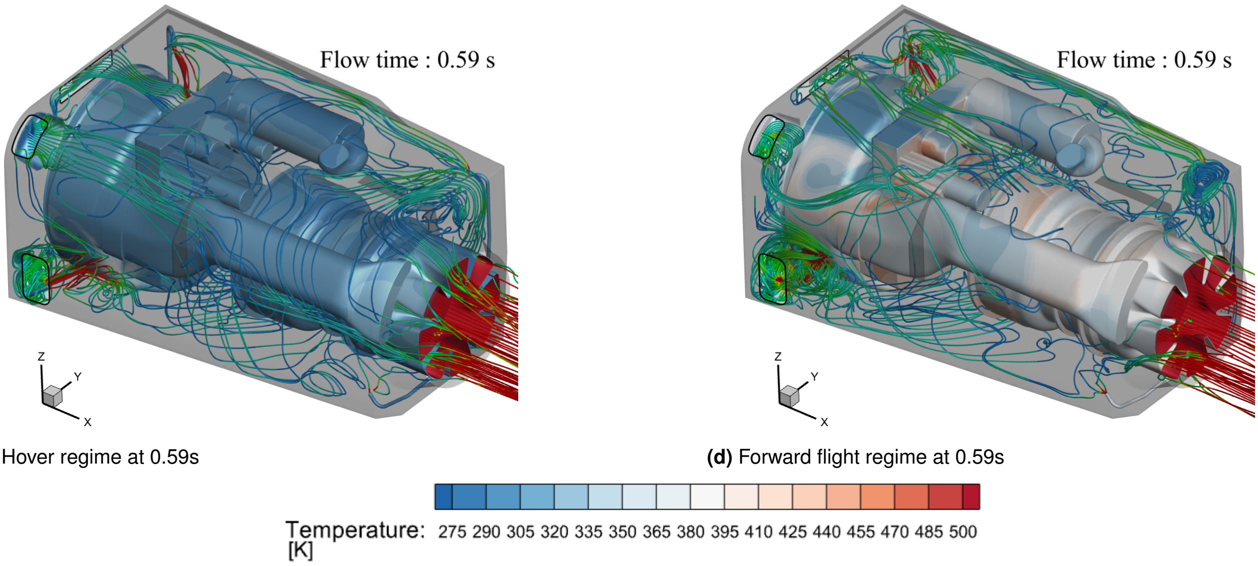

(b) Hover regime at 0.59s

(d) Forward flight regime at 0.59s

Figure 11. Stream tubes emanating from the two scoops and NACA inlet (refer to Figure 5) at 0.39 s and 0.59 s. Contours of velocity magnitude are imposed on the stream tubes. The left column depicts cases where the boundary conditions are prescribed for a hover regime while the right column shows the conditions for a forward flight regime.

the streamtubes. As mentioned in Section , realistic boundary conditions were used at the pressure inlets to create the complex velocity fields in the domain. The trajectory of the droplets are dependent on the swirls portrayed by the streamtubes. Returning to the discussion on the concentration of halon in the vicinity of nozzle D at 0.39 s for the forward flight case, it can be observed that there indeed exists a recirculation zone in the region mentioned. This confirms the earlier suspicion pertaining to the halon concentration near nozzle D. It is also worth noting of the swirls existing near scoop inlets 1 and 2 for the forward flight case that is not seen for the hover case at 0.39 s.

At 0.59 s in Figure 11, high speed regions of 60 m/s can be seen in the vicinity of nozzles A and B. This speed-up was not apparent when nozzles A and B were not injecting halon into the nacelle, suggesting the active interaction between the dispersed and continuum phases. Significant speed-ups were not observed at the regions near nozzle C and D. It was earlier mentioned that the halon spray is directed more towards the engine for the hover case compared to the forward flight case in vicinity of nozzle C at 0.59 s (refer to Figure 9). The streamtubes in Figure 11 at 0.59 s for the hover case shows a local recirculation zone near nozzle C. Its presence would influence the role it plays in the re-direction of the spray towards the engine as this was not evident for the forward flight case at 0.59 s.

When nozzles C and D stop injecting halon liquid into the nacelle at 1.57 s in Figure 12, the streamtubes indicate regions of high velocity compared to flow times at 0.39 s and 0.59 s. It was also observed that the swirls at near nozzle C for the forward flight case has ebbed, giving indication of the continuous change of the flow dynamics within the nacelle with time.

According to the certification rules of ESA-CS29[36], it has to be shown that the discharge of the extinguishing agent provide a concentration capable of extinguishing fire and

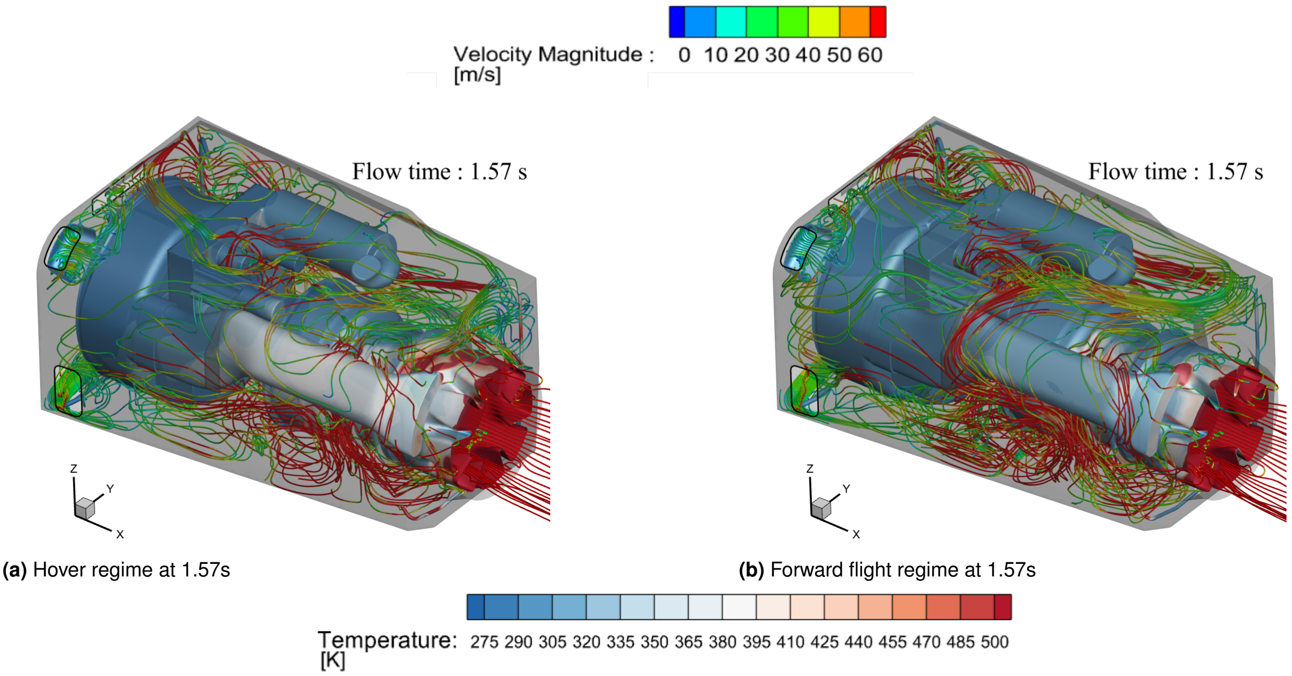

(a) Hover regime at 1.57s

(b) Forward flight regime at 1.57s

Figure 12. Stream tubes emanating from the two scoops and NACA inlet (refer to Figure 5) at 1.57 s. Contours of velocity magnitude are imposed on the stream tubes. The left column depicts cases where the boundary conditions are prescribed for a hover regime while the right column shows the conditions for a forward flight regime.

minimize the probability of re-ignition. The FAA Advisory Circular 20-100[37] states that the concentration of Halon 1301 should be greater than 6 % by volume for a period of 0.5 s to extinguish a fire.

To show this, we first identify four planes shown in Figure 13. The locations of the planes are based on the suggestion of the FAA Advisory Circular 20-100. Once the planes are selected, we identify the points (probes) on the individual planes as shown in Figure 14. The probe locations are again recommendations from FAA Advisory Circular 20-100 (referred to as four-ring sampling probe positioning[37]) .

Once the probe locations have been identified, the volume fraction of Halon 1301 in the nacelle can be plotted against time at these locations. The volume fraction can be computed using the following relation[38]:

$$v_h = m_f/[m_f + (1 - m_f)(M_h/M_a)] \tag{14}$$

where v_h is volume fraction, m_f is mass fraction of halon vapour, M_h is molecular weight of halon and M_a is the molecular weight of air.

The results for the volume concentration of halon vapour in the engine nacelle at the designated probe locations are shown in Figure 15 and Figure 16. The horizontal line at 6 % volume fraction was plotted to show the minimum concentration required for certification. All the plots displayed an erratic behavior before 3.6 s before monotonically descending to low (6% or less) volume fraction levels. The highest concentration was seen at P1 in Figure 15 for both the hover and forward flight cases but this is not surprising as the point is near one of the spray nozzles. At location P3, between the time period of around 2.2 s to 3.5 s, the volume fraction was below 6% for the forward flight case. The low levels of volume fraction was also observed at location P7 in Figure 16. This time however, the low levels of concentration occurred for both forward flight and hover regime. The rest of the locations do not display low concentrations when the halon sprays were active. The average of the volume fraction for P1 to P11 is shown in Figure 16.

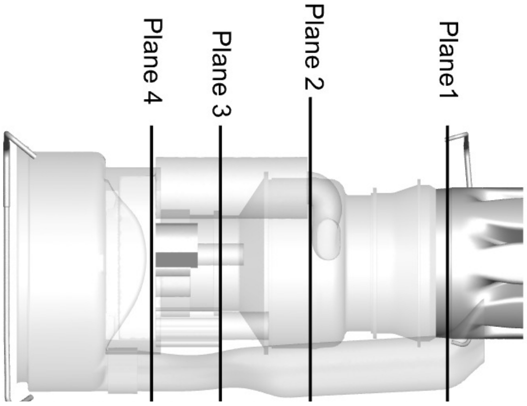

Figure 13. Locations of the planes used to define the points for volume fraction analysis.

V: Conclusions

This paper reports the modelling of the injection of Halon 1301 into an engine nacelle for two flight regimes, namely the forward flight and hover. A one dimensional pipe flow code was developed to simulate the transmission of a two-phase mixture of Halon 1301 and nitrogen from the bottle source to the nozzles of a multi-branch system. This is to obtain the boundary conditions needed for the spray simulations. To create a realistic flow setting, external flow calculations involving the VBM are simulated and provided

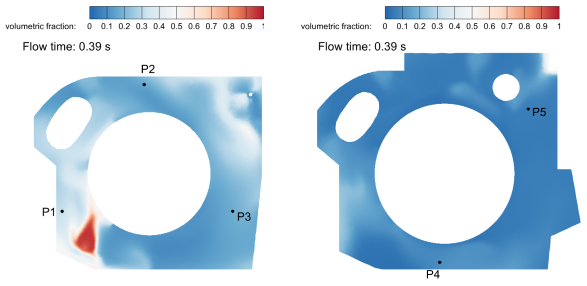

(a) Plane 1 **(b)** Plane 2

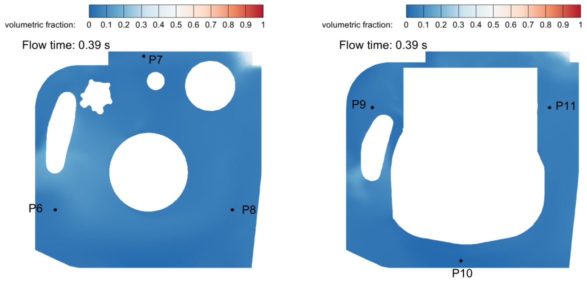

(c) Plane 3 **(d)** Plane 4

Figure 14. Location of the points used for volume fraction analysis. Refer to Figure 13 for the location of each plane.

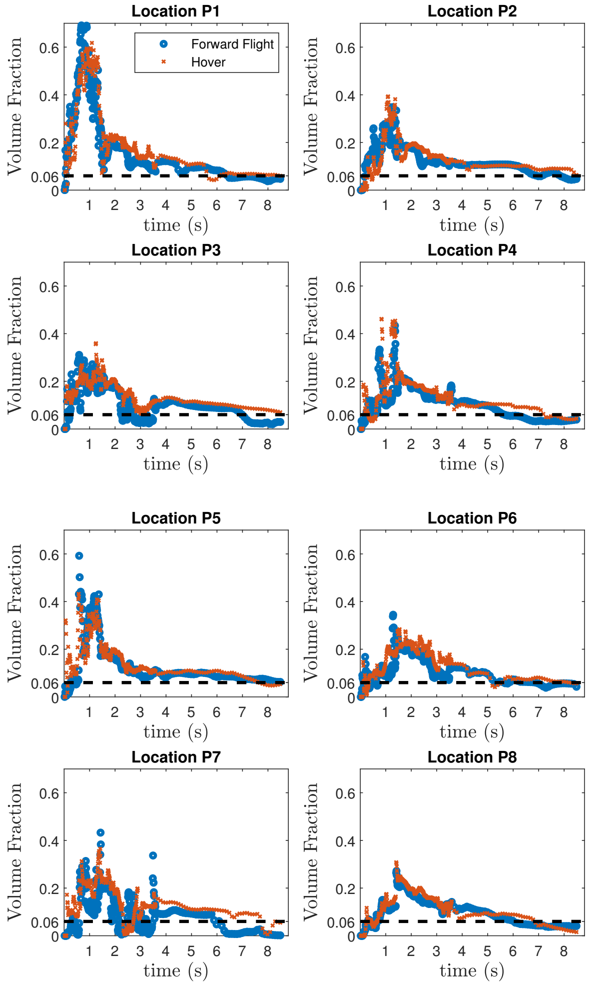

Figure 15. Halon 1301 concentration by volume within the engine nacelle for points P1-P8 (refer to Figure 14 for exact locations of the points).

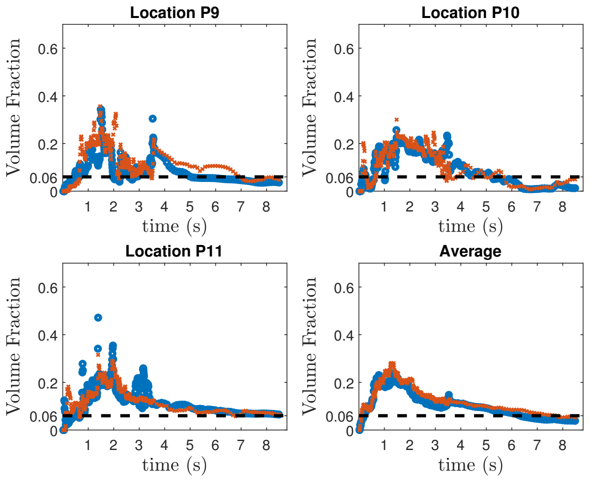

Figure 16. Halon 1301 concentration by volume within the engine nacelle for points P9-P11 (refer to Figure 14 for exact locations of the points). The average concentration is shown in the bottom right of the figure.

as boundary conditions at the pressure inlets of the nacelle. The VBM simulations included a forward flight case as well as a hover regime. It was shown that the two cases showed significant differences in the trajectory of the spray dynamics especially in the vicinity of nozzle D.

The streamtubes within the engine nacelle highlighted the complex flow physics with large recirculation zones being more prevalent for the forward flight regime. The presence of recirculation zones clearly affected the spread of the droplets and was even severe enough to deflect the direction of the droplets towards the engine instead of the its general direction for the hover regime, in the vicinity of nozzle C. In terms of wall temperature on the engine, the forward flight regime showed more regions of high temperatures at 0.39 s compared to the hover case. The engine for the forward flight case eventually cooled at 1.57 s (when nozzles C and D stopped injecting halon) and reached a temperature of about 304 K from 485 K. This could be due to the cooling streams as well as the evaporation of the erstwhile droplets. Finally, plots of the agent concentration by volume within the nacelle at different locations showed the erratic behavior during the injection period but was generally able to meet the certification rules of ESA-CS29.This is despite the low concentration levels at location P3 for the forward flight case as well as at P7 for both regimes.

This study aims to provide a first approximation to the flow dispersion characteristics of Halon 1301 in an engine nacelle under different flight regimes. Given the restriction on Halon 1301 and its detrimental impact on the environment, flight tests and experiments are hard to come by. The above results would aid in the certification process and would also allow for a more efficient design in the engine bay in the fight to put out fires more quickly. The video for the simulations has been uploaded online and can be found at the following url: https://www.youtube.com/watch?v=ZmUaLU8rNKQ

Declaration of competing interest

The authors declare that they have no known competing interest.

Acknowledgements

The authors acknowledge the support provided for this study by Leonardo-Finmeccanica Helicopter division.

References

1. Zhuang L, Lu SX, Sun ZY, Wang J, Kang Q. Study of flame height of aviation fuel pool fires. Journal of University of Science and Technology of China. 2009;7:763.
2. Hurley MJ. SFPE handbook of fire protection engineering. Springer; 2015.
3. Ingerson DA. Simulating the distribution of Halon 1301 in an aircraft engine nacelle with HFC-125. Springfield, Virginia: National Technical Information Service.; 1999.
4. Tapscott RE, Speitel LC. Options to the use of halons for aircraft fire suppression systems-2002 update. William J. Hughes Technical Center, Atlantic City NJ; 2002.
5. Payri R, Gimeno J, Martí-Aldaraví P, Carvallo C. Parametrical study of the dispersion of an alternative fire suppression agent through a real-size extinguisher system nozzle under realistic aircraft cargo cabin conditions. Process Safety and Environmental Protection. 2020;141:110-22.
6. Elliott DG, Garrison PW, Klein GA, Moran KM, Zydowicz MP. Flow of nitrogen-pressurized Halon 1301 in fire extinguishing systems. JPL Publication 84-62, Jet PropulsionLaboratory, California Institute of Technology, Pasadena, California. 1984.
7. DiNenno P, Forsseli E, Ferreira M, Hanauska C, Johnson B. Modeling of the flow properties and discharge of halon replacement agents. NFPA Tehnical Papers. 1994:117-29.
8. Amatriain A, Rubio G, Parra I, Valero E, Andreu D, Martín PM. Mathematical modeling of nitrogen-pressurized Halon flow in fire extinguishing systems. Fire Safety Journal. 2021;122:103356.
9. Snegirev A, Lipjainen A, Bondarenko D, Lehugeur B. Transient spray development in the discharge of a fire extinguishing agent. In: Proc. of the Sixth International Seminar on Fire and Explosion Hazards (FEH6). University of Leeds. Proc. of the Sixth International Seminar on Fire and Explosion Hazards (FEH6); 2011. .
10. Kurokawa FY, de Andrade CR, Zaparoli EL. Modeling of aircraft fire suppression system by the lumped parameter approach. Aircraft Engineering and Aerospace Technology: An International Journal. 2016;88(4):535-9.
11. Zaparoli E. Numerical simulation of an aircraft cargo compartment fire suppression system using CFD tool. In: Proceedings of the 19th International Congress of Mechanical Engineering, Gramado, Brazil; 2009. p. 15-20.
12. Li Q, Li Z, Chen R, Zhang Z, Ge H, Zhou X, et al. Numerical Study on Effects of Pipeline Geometric Parameters on Release Characteristics of Gas Extinguishing Agent. Symmetry. 2021;13(10):1766.
13. Hewson J, Tieszen S, Sundberg W, Desjardin P, et al. CFD modeling of fire suppression and its role in optimizing suppressant distribution. In: Proceedings of the halon options technical conference; 2003. .
14. Wang Z, Jia F, Galea ER, Ewer J. Computational fluid dynamics simulation of a post-crash aircraft fire test. Journal of Aircraft. 2013;50(1):164-75.
15. Colebrook CF, White CM. Experiments with fluid friction in roughened pipes. Proceedings of the royal society of london Series A-Mathematical and Physical Sciences. 1937;161(906):367-81.
16. Chen NH. An explicit equation for friction factor in pipe. Industrial & Engineering Chemistry Fundamentals.

1979;18(3):296-7.

17. Müller-Steinhagen H, Heck K. A simple friction pressure drop correlation for two-phase flow in pipes. Chemical Engineering and Processing: Process Intensification. 1986;20(6):297-308.
18. Ortiz-Vidal LE, Mureithi N, Rodriguez OMH. Two-phase friction factor in gas-liquid pipe flow. Revista de Engenharia Térmica. 2014;13(2):81-8.
19. Shannak BA. Frictional pressure drop of gas liquid two-phase flow in pipes. Nuclear Engineering and Design. 2008;238(12):3277-84.
20. Hicks TG. Handbook of mechanical engineering calculations. McGraw-Hill Education; 2006.
21. Yuan C, Wang Y, Li H, Dai C, Lu S, Zhang H. Simulation study of filling conditions for aircraft fire suppression systems. CSAA/IET International Conference on Aircraft Utility Systems; 2022. .
22. Fluent A. Ansys fluent theory guide. ANSYS Inc, USA. 2021;15317:724-46.
23. Novozhilov V. Computational fluid dynamics modeling of compartment fires. Progress in Energy and Combustion science. 2001;27(6):611-66.
24. Jin J, Pan R, Li Q, Chen R. Effects of release pressure on the transportation characteristics in pipeline and the diffusion behaviors in enclosure space of typical gas extinguishing agent. Journal of Loss Prevention in the Process Industries. 2021;70:104441.
25. Ranz RE, marshall WR. Vaporization from drops, part i-ii. Chem Eng Prog. 1952;48(3):141-80.
26. Haenlein A. Disintegration of a liquid jet. NASA Tech Memorandum, Washington, no. 659; 1932.
27. Lefebvre AH, McDonell VG. Atomization and sprays. CRC press; 2017.
28. Di Nicola G, Di Nicola C, Moglie M. A new surface tension equation for refrigerants. International Journal of Thermophysics. 2013;34(12):2243-60.
29. Lechner MD, Wohlfarth C, Wohlfarth B. Surface tension of pure liquids and binary liquid mixtures. Springer; 2015.
30. Liu S, Xie Y, Chen M, Zhu J, Day R, Wu H, et al. Prediction of the release process of the nitrogen-extinguishant binary mixture considering surface tension. Journal of Thermal Analysis and Calorimetry. 2020:1-15.
31. Lee MJ, Tien DL, Shao CT. Thermophysical capability of ozone-safe working fluids for an organic Rankine cycle system. Heat Recovery Systems and CHP. 1993;13(5):409-18.
32. Rosin P, Rammler E. The laws governing the fineness of powdered coal. Journal of the Institute of Fuel,. 1933;7:29–36.
33. Roache PJ. Verification and validation in computational science and engineering. vol. 895. Hermosa Albuquerque, NM; 1998.
34. Ruith M. Unstructured, multiplex rotor source model with thrust and moment trimming-Fluent's VBM model. In: 23rd AIAA applied aerodynamics conference; 2005. p. 5217.
35. Finnerty AE, Peregino PJ, Vande Kieft LJ, Tucker JR, Weiland DE, Sheinson RS, et al. Fires Experienced And halon 1301 Fire Suppression Systems In Current WeaponSystems. Report SURVIAC TR-00-007, United States Air Force – Air Force ResearchLaboratory – Survivability and Safety Branch; 2003.
36. Certification specifications and acceptable means of compliance for large rotorcraft. CS-29 Amendment 7, European Union Aviation Safety Agency. 2019.
37. Ferrarese JA. General guidelines for measuring fire-extinguishing agent concentrations in powerplant compartments. Federal Aviation Administration. 1977.
38. Lee J. Simulation method for the fire suppression process inside the engine core and APU compartments. In: The Fourth Triennial International Aircraft Fire and Cabin Safety Research Conference, Portugal. Citeseer; 2004. .

Appendix A: DPM Injection Properties used for the simulations.

Fluent Injection properties

Feature	Value/Type Used
Injection Type	Cone
Number of streams	300
Particle Type	Droplet
Diameter Distribution	Rosin-Rammler
Material	Halon 1301 Liquid Droplet (defined by user)
Evaporating Species	cbrf3<g> (defined by user)
Cone Type	Solid-cone with uniform massflow distribution
Minimum Diameter of Particles (m)	1e-6
Maximum Diameter of Particles (m)	8e-5
Mean Diameter of Particles (m)	5e-5
Spread Parameter	1.8
Number of Diameters	20
Drag Law	non-spherical
Shape Factor	0.171
Stochastic Tracking	Discrete Random Walk Model